Award Number 07HQGR0030

SMALL SCALE FAULT STRUCTURE FROM SAFOD AREA MICROEARTHQUAKES COMBINING WAVEFORM CORRELATION AND SHEAR WAVE SPLITTING ANALYSIS

Volker Oye

NORSAR

Instituttveien 25
2007 Kjeller
Norway

Tel.: +47 – 6380 5943
Fax.: +47 – 6381 8719

Email: volker@norsar.no

March 31st, 2008

Award Number 07HQGR0030

SMALL SCALE FAULT STRUCTURE FROM SAFOD AREA MICROEARTHQUAKES COMBINING WAVEFORM CORRELATION AND SHEAR WAVE SPLITTING ANALYSIS

Volker Oye

NORSAR, Instituttveien 25, 2007 Kjeller
Norway

Tel.: +47 – 6380 5943; Fax.: +47 – 6381 8719
Email: volker@norsar.no

Abstract

In this report we describe the twofold automatic event detection procedures that have been applied combined SAFOD and HRSN data. The first is a combination of real-time SAFOD waveform data recorded downhole at 4000 Hz that is combined with a pool of real-time HRSN and NCSN detection time picks. The second is an automatic off-line analysis of 43 days continuous waveform data from SAFOD and all HRSN stations. The detection capability of the network has been improved significantly when based on SAFOD high-frequency recordings and combined with a generalized beam forming algorithm to form and assign common events. A sequence of micro-aftershocks (M_w~-2) has been detected automatically and manually reprocessed and located. The characteristics of this aftershock sequence seem to satisfy the general relations as described in Omori's law.
A semi-automatic procedure to estimate shear-wave splitting delay times and polarisation angles is described and for a selection of microearthquakes in the closer SAFOD area this procedure has been applied in order to deduce spatially varying anisotropy. First results indicate some ray-path directions in the South of SAFOD with almost zero-splitting, whereas in the North-Northwest of SAFOD, heterogeneities in the pattern of anisotropy seem to be at their maximum.

Introduction

The San Andreas Fault Observatory at Depth (SAFOD) is part of the National Science Foundation's EarthScope Project and in the summer of 2002, a 2.2 km deep vertical Pilot Hole (PH) was drilled about 1.8 km SW of the surface trace of the San Andreas Fault, close to Parkfield and was instrumented to prepare for SAFOD (Hickman et al., 2004). In the summer of 2005, the SAFOD Main Hole (MH) was then drilled, beginning as a vertical borehole, then deviating at a depth of 1.5 km to the NE and ending at a total vertical depth of 3.1 km NE of the San Andreas Fault zone (Figure 1). The target of the borehole was a repeating earthquake source zone that was earlier identified by permanent and temporary dense surface seismic networks as well as with instruments in the SAFOD PH (e.g. Thurber et al., 2004; Oye et al., 2004; Imanishi and Ellsworth, 2006). From geophysical logs as well as the analysis of cuttings from the deviated section of the MH, multiple narrow (<30 m) zones have been identified that are characterized by

very low seismic P- and S-wave velocities. These zones probably represent fault core zones, while they belong to a broader (~200 m wide) zone of lower velocities that probably represents the damage zone (Ellsworth et al., 2007a and 2007b).

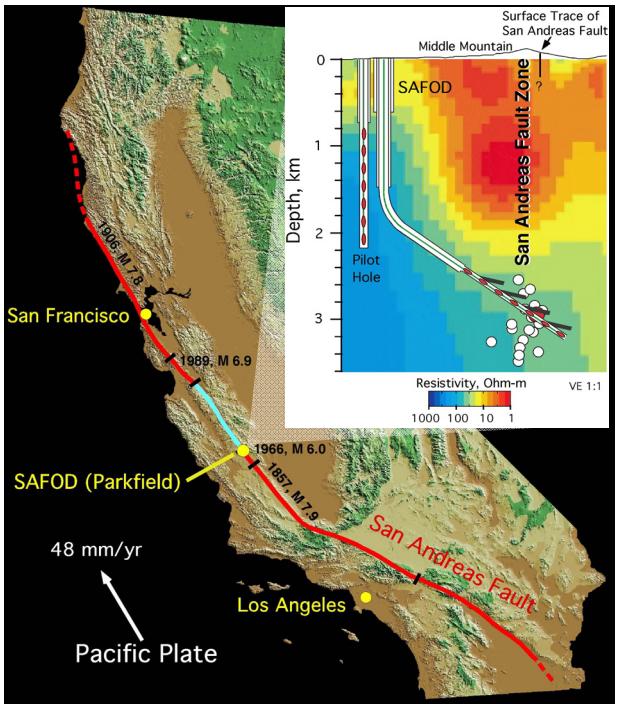

Figure 1 *Map of California showing the San Andreas Fault and indicating the surface traces of historic large earthquakes. The SAFOD drill hole is located close to the town of Parkfield, just at the SE end of the creeping and microseismically active segment of the San Andreas Fault (blue line). The inset shows a sketch of the SAFOD drilling plan of the pilot and main hole superimposed on electrical resistivity structure (Unsworth and Bedrosian, 2004).*

From early 2006 on, the SAFOD main hole had been instrumented with high-frequency geophones and accelerometers. Since the downhole instruments are only about a few hundreds of meters away from some of the target microearthquakes as compared to about 3-10 km for the High Resolution Seismic Network (HRSN; Figure 2), the detection threshold on the downhole instruments is significantly lower than on the HRSN, which became obvious from the continuous analysis of SAFOD PH and MH recordings.

In this report we describe the real-time data processing of the high sampling rate downhole stations that are combined with a pool of detection times of nearby HRSN stations and of stations from the Northern California Seismic Network (NCSN). We also took advantage of 43 days of continuous data recording in the PH and MH and combined them with full waveform data from the HRSN stations.

We then describe the data preparation, the automatic routines for event detection, phase picking and event localization using a 3D velocity model and describe the resulting catalog of microearthquakes. In some more detail a sequence of 36 micro-aftershocks following an M 1.8 earthquake is presented. In the second part, a semi-automatic procedure to determine shear-wave splitting has been developed and applied to events that were selected from the microearthquake catalog. The results reveal relatively strong changes in the amount of anisotropy in the vicinity to the SAFOD drill holes.

The seismic network and data handling

The HRSN is one out of several seismic networks in northern and central California. It has been expanded to a total number of 13 stations in 2001 and is operated by the University of California Berkeley Seismological Laboratory (BSL). Most stations are installed at a depth of about 250 m and contain 3-component seismometers sampled at 250 Hz. The SAFOD mainhole has been equipped with 15 Hz geophones sampled at 4000 Hz. The data are managed using the Earthworm software developed by the USGS. Selected channels are downsampled and integrated in real-time into the NCSN processing system. In addition the microseismic monitoring software (MIMO) developed by NORSAR (Oye and Roth, 2003; Oye et al., 2005) has been installed to process the high-frequency data directly and to detect and localize seismic events too small to be observable on the NCSN. The MIMO software processes the raw 4000-Hz SAFOD downhole data and combines detections and phase picks with automatic, unassociated phase picks (HRSN detections) that are provided in near-real time by Earthworm modules from the HRSN stations and nearby NCSN stations.

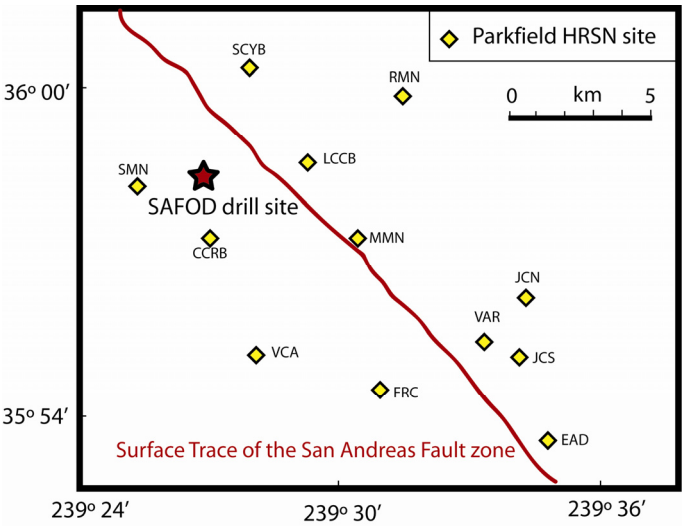

Figure 2 *Location of the SAFOD drill site and the 13 stations of the High Resolution Seismic Network (HRSN), installed in shallow boreholes. There is one more station further SE along the San Andreas Fault.*

The first step is to sort all detections in time and to form segments with a user-specified minimum number of detections and with a duration that depends on the maximum travel time between the stations. There may still be multiple events within a segment, but in that way the amount of detections to loop through has been minimized. The second step requires a forward computation of travel time tables of P and S waves in a given velocity model (for the detection processing we used a homogeneous velocity model with v_p=5.5 km/sec and v_s=3.05 km/sec). The sources are defined on a coarse 3D grid of potential earthquake locations and the receivers are defined as the actual station network. In this study we limited the detection area to the SAFOD area, using a uniform grid distance of 2 km. With the SAFOD drill site as the centre of the coordinate system, the central grid points with calculated travel times started at 2 km West and 4 km South of SAFOD, reaching 4 km East and 4 km North of the SAFOD drill site. The depth starts at mean sea level and reaches until 6 km below msl. The dimensions of the grid of pre-calculated travel times have been chosen to reduce on-line computation time and to limit the detections to near-SAFOD events.

The next steps after pooling, sorting and segmenting the HRSN and SAFOD detections are also presented in a general flow chart for the association algorithm for each segment (Figure 3). The first loop is over all detections in the current segment, and the second loop is over the 3D grid of potential earthquake locations. For each element in the two loops, the theoretical detection time is compared with the observed detection time at a given station. If the observed detection matches with the theoretical detection, this detection is associated to an event at the actual potential earthquake location. In addition, the misfit between the observed and the theoretical detection times are computed and the parameters are stored.

When the two loops have finished, the event with most detections and the smallest travel time misfits is assigned and all related detections are removed from the segment. If there are fewer detections left in the segment than the required minimum number of detections, the algorithm continues with the next segment, otherwise a second event may be assigned from the current segment. This kind of event association technique is based on the generalized beam forming, which is well-known in array seismology (Ringdal and Kværna, 1992). The event association algorithm also provides an improved start location for the hypocenter location routine of the MIMO system that is generally determining accurate phase picks of P and S waves instead of detection times that are often simply based on signal-to-noise ratios.

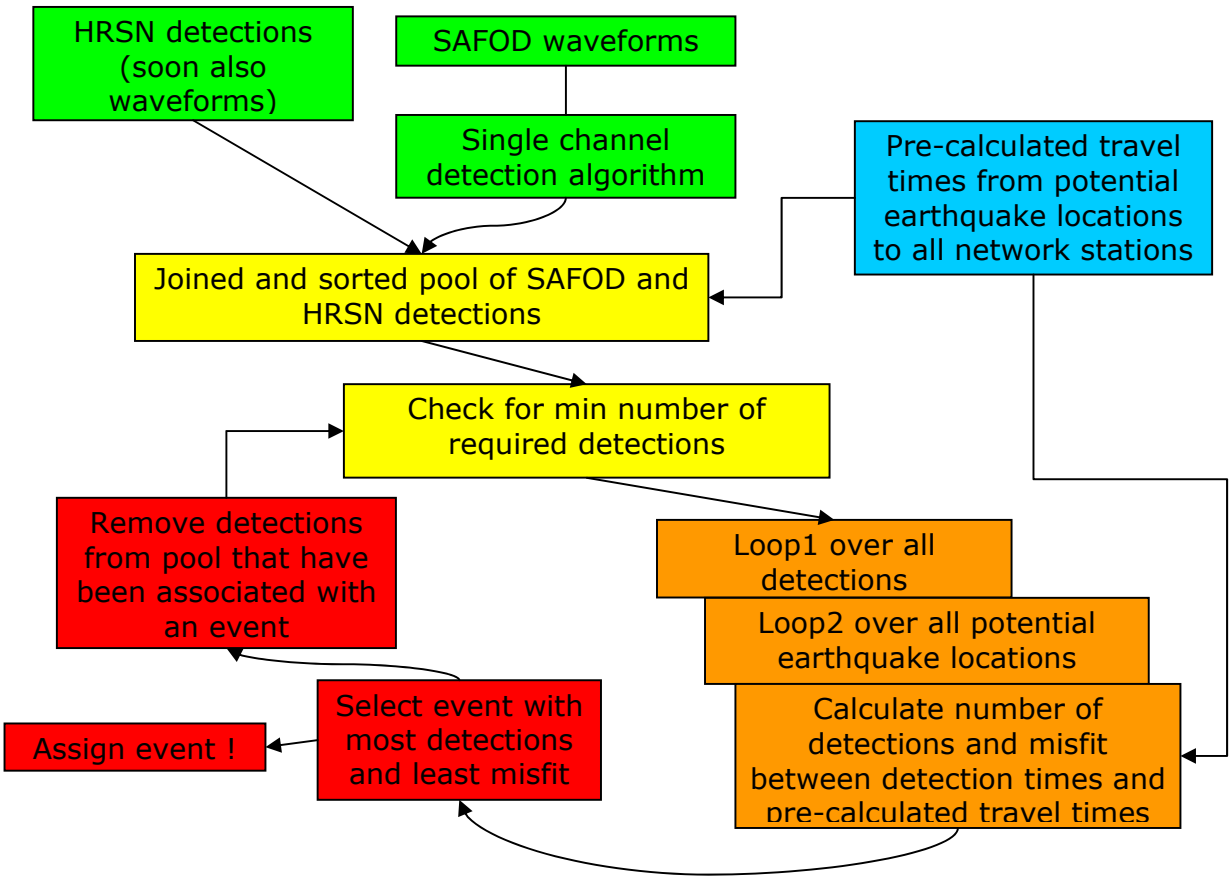

Figure 3 *Flow chart for the association of detections to a seismic event.*

Due to several technical problems with the downhole installations at the SAFOD MH, there have been significant gaps in the data flow and therefore the online processing and event detection could not be conducted for the whole period of the project. Therefore we took advantage of the longest continuous period of 43 days recording in the SAFOD PH and MH, starting on August 3rd and reaching until September 14th 2006. We kindly received two LTO3 tapes of about 600 Gbytes of continuous data including PH, MH and all HRSN stations. The data recorded in the PH (at ~1050 m depth) and MH (at ~2650 m depth) were sampled at 4000 Hz and stored in SEG2 format in files of 30 seconds record length each. The data from the HRSN, recorded on broadband seismometers and installed in shallow boreholes of approx. 250 m depth, sampled at 250 Hz and were shipped in MiniSEED format. In order to process these two data sources automatically, they needed to be merged into one data format, and the file record length, i.e. its size should not become too large. The data segmentation of the MiniSEED files and conversion into SAC was achieved with help of the "qmerge" and "ms2sac" routines. Since NORSAR's microseismic processing software is able to read SEG2 and SAC data, we wrote some additional routines to merge the SEG2 and SAC files to 1 minute segments of data and further used these for the automatic processing.

Event processing and localization

The processing flow is similar to the one described in Oye and Roth (2003), and comprises the following automatic steps: 1) Detection; 2) Event association; 3) P-wave onset picking; 4) P-wave polarization analysis; 5) Trace rotation into the ray coordinate system and S-wave onset picking on traces with improved signal-to-noise conditions; 6) Localization using the master event technique or a directed grid search depending on the velocity model.
The merged data set of SAFOD and HRSN data needed special treatment with respect to automatic processing. This is not only due to the large differences in the sampling rates, which is a factor of 16 between the HRSN and the SAFOD sampling rates, but it is also due to the distance to the observed events and the local site conditions, e.g. on which side of the SAF is the station positioned and where did the event occur. The frequency content of the recorded signals varies dramatically as for example shown on Figure 4. Therefore the selection of the technical parameters, which for example for the detection are the time window lengths for the 'short term average' and 'long term average', band-pass filter options and the signal-to-noise ratio thresholds can be changed individually for all geophones. The event association works as described in the previous paragraph (Figure 3) and serves also as start location for the iterative location procedure.

The phase onset picking is for P- and S-wave onsets is based on an auto-regressive model that is constructed upon a noise window. The difference between the P and S wave picking lies in the selection of such time windows. Since each new phase onset represents a change in the amplitude and frequency characteristics and because the auto-regressive model represents the noise characteristics of the trace, using a combination of error-prediction filtering and the Akaike Information Criterion, the phase onset can be determined (Figure 5). For the determination of the S-wave onset, the P-wave polarization analysis is used to rotate the channels in the ray coordinate system and only the two traces perpendicular to the longitudinal direction are used. The localization procedure is different for homogeneous and inhomogeneous velocity models. In case of a homogeneous velocity model, the iterative master event technique is applied, because the theoretical arrival times and angles can be calculated analytical. In the case of a 3D velocity

model we apply ray tracing to construct lookup tables for arrival times and angles. Figure 6 shows an example of 3D ray tracing for the velocity model that we used for the localization of the microearthquakes in this study (200702IT5, provided by Steve Roecker). P- and S-wave travel time tables and arrival angles (backazimuth and incidence) are calculated for each seismic station and for a regular grid of potential microearthquake locations with 50 m grid distance (161 grid points along the SAF, 121 perpendicular to the SAF, and 121 with depth). The directed grid search is then conducted for a selection of P- and S-travel times, S-P differential travel times and arrival angles backazimuth and incidence. Though calculated for all stations, the arrival angles were usually only applied for the two MH seismometers, especially in case of little or no detections on the HRSN network.

The weighting of the different data as input to the localization was steered by the assumed data variance. Therefore the MH stations had the strongest influence in the localization, followed by the close PH and the HRSN stations CCRB, SMNB, LCCB, SCYB and also VCAB and MMNB, with less weight on the remaining stations. The P-wave onsets were generally observed 3 to 5 times better than the S-wave onsets and the weighting was accordingly.

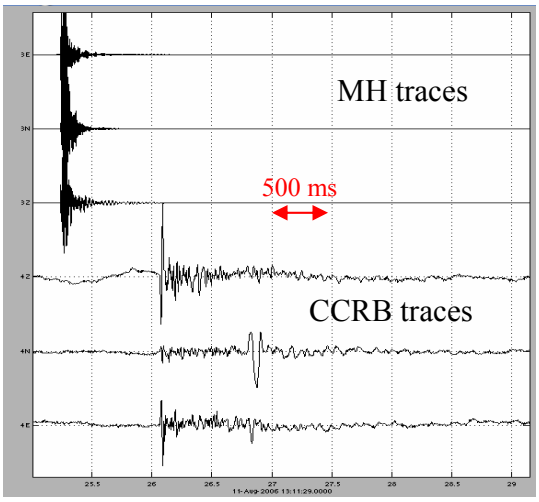

Figure 4 *Example of a SAFOD MH seismogram sampling at 4000 Hz (upper 3 traces) and the corresponding seismogram at the station CCRB of the HRSN sampling at 250 Hz (lower 3 traces). Note that the difference in the recorded signal frequency is not only due to the sampling rate, but to high degree due to the distance of the station to the event and the effective attenuation of the high-frequency part of the signal spectrum.*

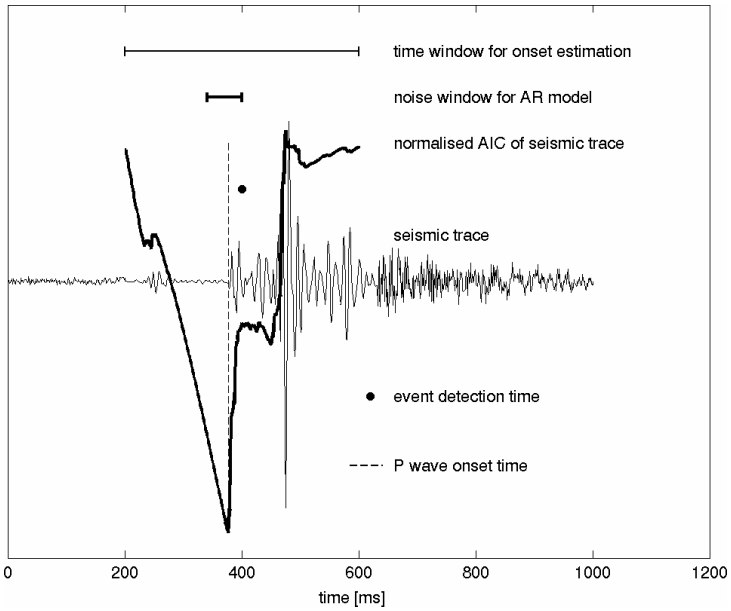

Figure 5 *P-wave onset time estimation using the Akaike Information Criterion (AIC). The time window for the onset estimation (analysis window) is centred around the event detection time (black dot). The auto-regressive (AR) model, representing noise statistics of the seismic trace, is calculated in a time window preceding the event detection time. The minimum value of the AIC calculated for the analysis window provides the exact P-wave onset time.*

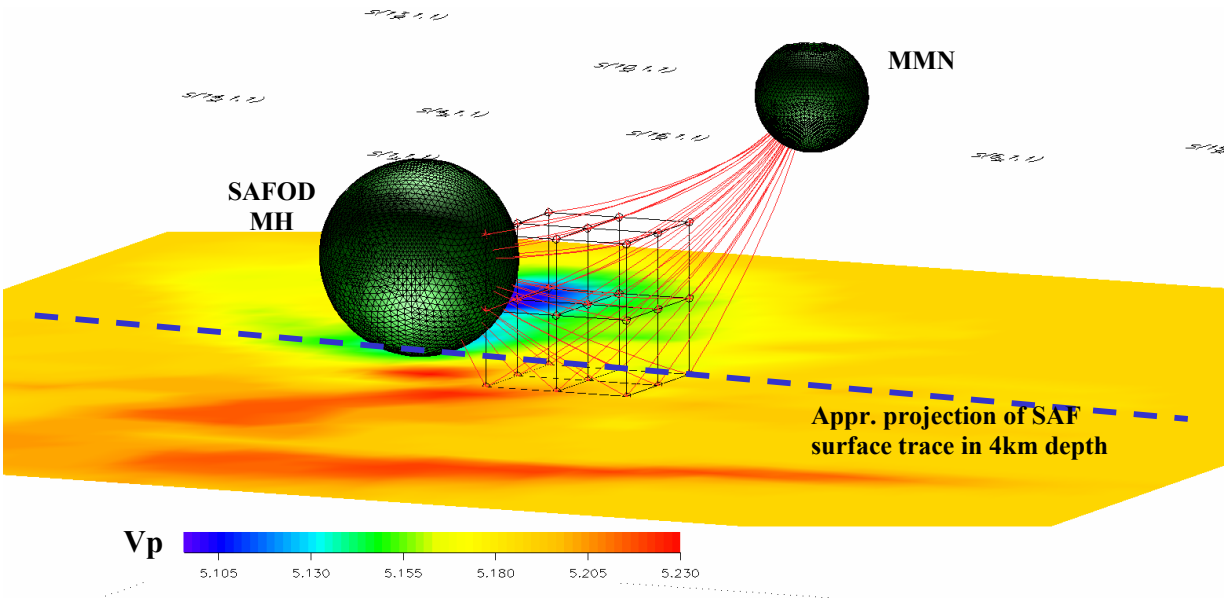

(A)

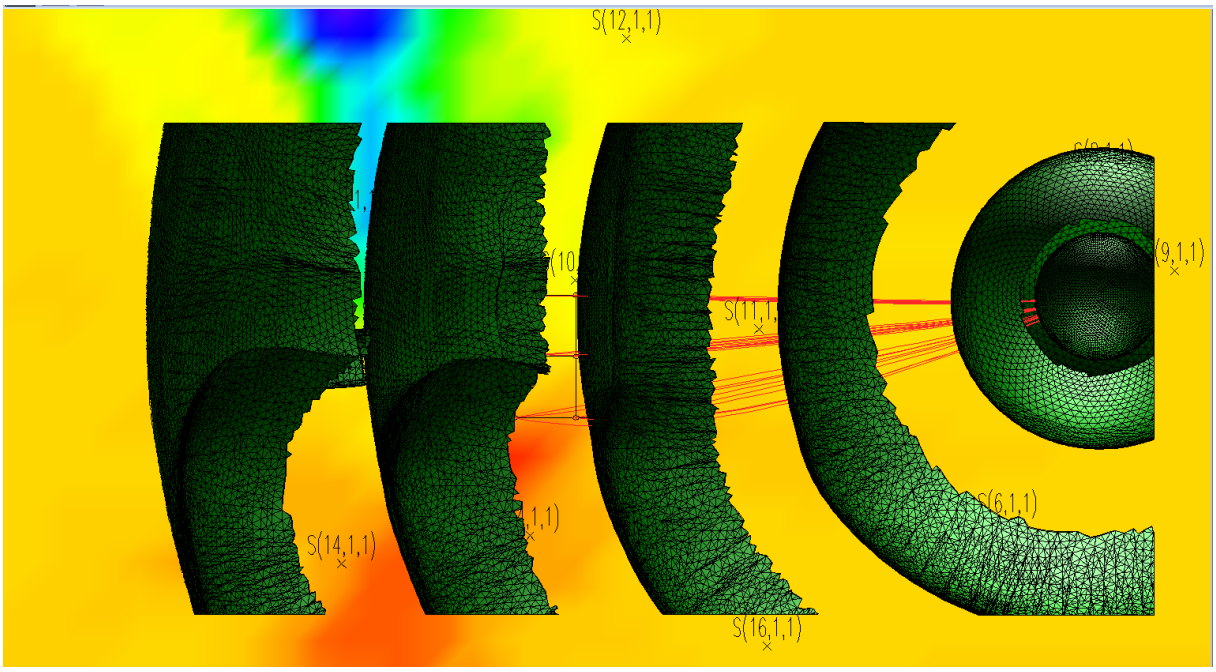

(B)

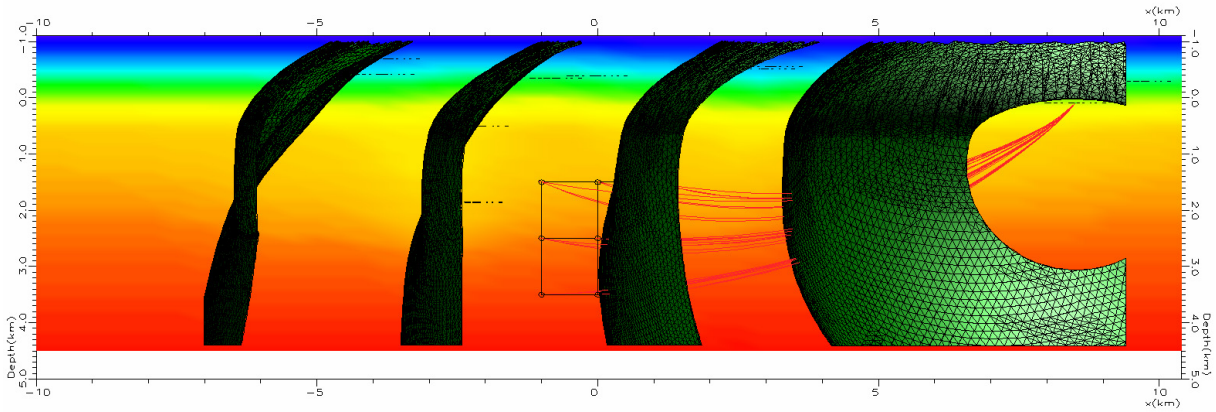

(C) **Vs [km/sec]**

Figure 6 *Example of NORSAR 3D ray tracing using the wavefront propagation technique. Wave fronts are plotted in green at different times and in addition the rays are plotted from the source to a selection of receivers (red lines and black squares, respectively). To save computation time, the principle of reciprocity is applied, i.e. waves are propagated from the receivers of the network (here MMN and SAFOD MH in (A) and VAR in (B) and (C)) to a dense grid of potential earthquake locations (161 x 121 x 121 cells with 50 m grid distance each, not plotted here). The used P- and S-wave velocity model that was used is colorcoded in the background and has been provided by Steve Roecker (200702IT5).*

Improved detection capability

In the 43 days of continuous monitoring, about 52 events were announced on the standard automatic search bulletin of the NCSN (chosen search parameters: events shallower than 10 km, within 35.8/36.1, -120.6/-120, all event types, including no reported magnitude). In comparison, we found with our automatic approach for the same period of time about 130 events with detections on both MH stations that have been associated with at least 10 other stations, about 320 events that have been associated with at least 3 other stations and about 375 events with at least 2 other stations (Figure 7). If we remove ¾ of the events that have been associated on more than 10 stations, because they might be wrongly identified and are in reality teleseismic or regional events, we still end up with more than 200 events that have been identified on both MH stations and on at least 3 other stations, and we only incorporate the HRSN stations here. This is almost 4 times as much as reported on the NSCN.

However, the direct comparison might be misleading, since the amount of required stations in order to assign an earthquake is probably higher for the NCSN than the 3 or 4 stations that were used in this study, so the direct comparison with numbers is not fully valid. Also note that NORSAR's MIMO software picked up more than 8000 tool-slipping events that certainly were only recorded with the MH seismometers. These tool-slipping events made it more difficult to identify microearthquakes that were only recorded with the MH stations, because we could not yet implement an automatic approach to distinguish between the tool-slipping events and "real" events, that were only recorded with the MH (although there have been some ideas and first trials for such automatic filtering, for example are the tool-slipping events dominant on the "in-hole" component of the 3C instruments). The few microearthquakes (about 36 events) that have so far been identified automatically on the two MH instruments only are aftershocks of an M1.8 earthquake that occurred on August 11th.

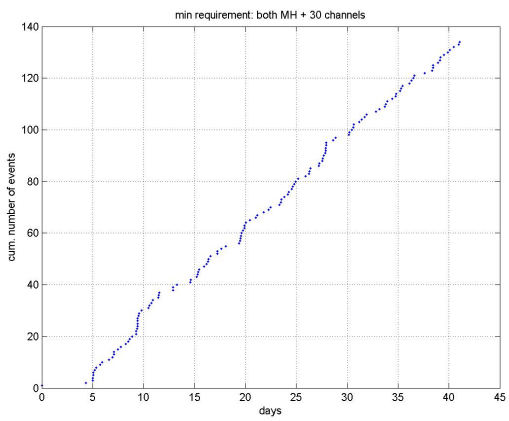

(A) detection on both MH and at least 10 other stations

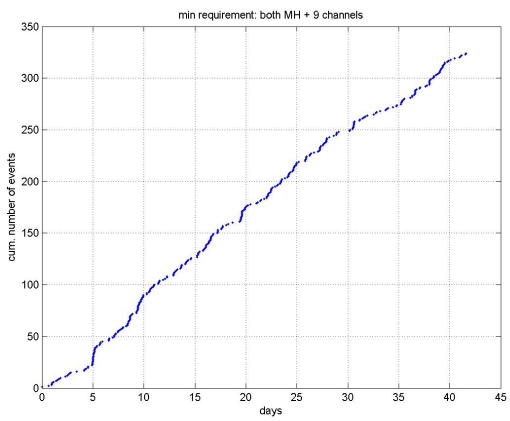

(B) detection on both MH and at least 3 other stations

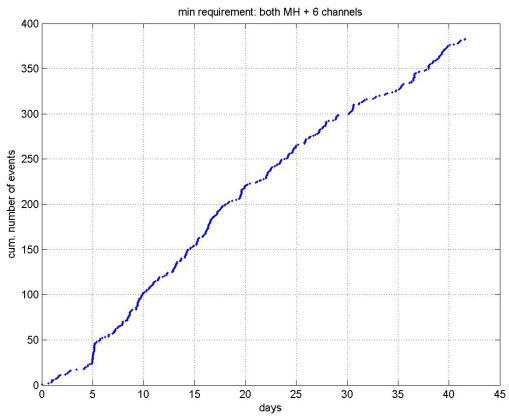

(C) detection on both MH and at least 2 other stations

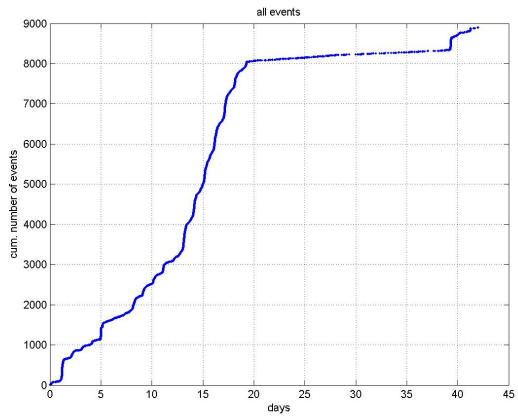

(D) detection on at least one MH station

Figure 7 *Cumulative sums of automatic event detections for the 43 days of continuous monitoring with the combined network of SAFOD and HRSN stations. The graphs (A) to (C) show a more or less constant microseismic activity level with a few days of higher activities, e.g. days 5, 10, 20 and 27. In graph (A) there have been identified about 20% of false detections that are due to larger, regional events, and where the later phases have been wrongly identified as matching detection patterns. Note the huge difference to graph (D), where a cumulative sum of almost 9000 events was detected. This high rate of detections is due to tool slipping in the MH, and the level of such slipping intensity differs significantly throughout the observation time, e.g. there are almost no slipping events from day 19 through day 38, but there are many such events on day 2 and 5. These tool slipping events have been disregarded in further analysis.*

Aftershock sequence of an M1.8 (micro-) earthquake

Following a small M1.8 earthquake on August 11th 2006 at 09:27:41.758, a sequence of aftershocks was registered at both MH stations and for 35 of these aftershocks, P and S wave onsets plus the polarization of the P-wave onset could be estimated and locations were determined (Figure 8). To avoid inaccuracies due to interpolation on the pre-calculated lookup tables with 50 m spaced grid points, we assumed a constant velocity model to determine the aftershock locations (vp = 5.5 km/sec, vp/vs=1.8) - the error will not be large due to the very short distances to the MH receivers. Figure 9 shows the distribution of the aftershocks with respect to frequency of occurrence, probing Omori's law and Figure 10 shows the waveforms of the first seconds after the M1.8 microearthquake with some first aftershocks.

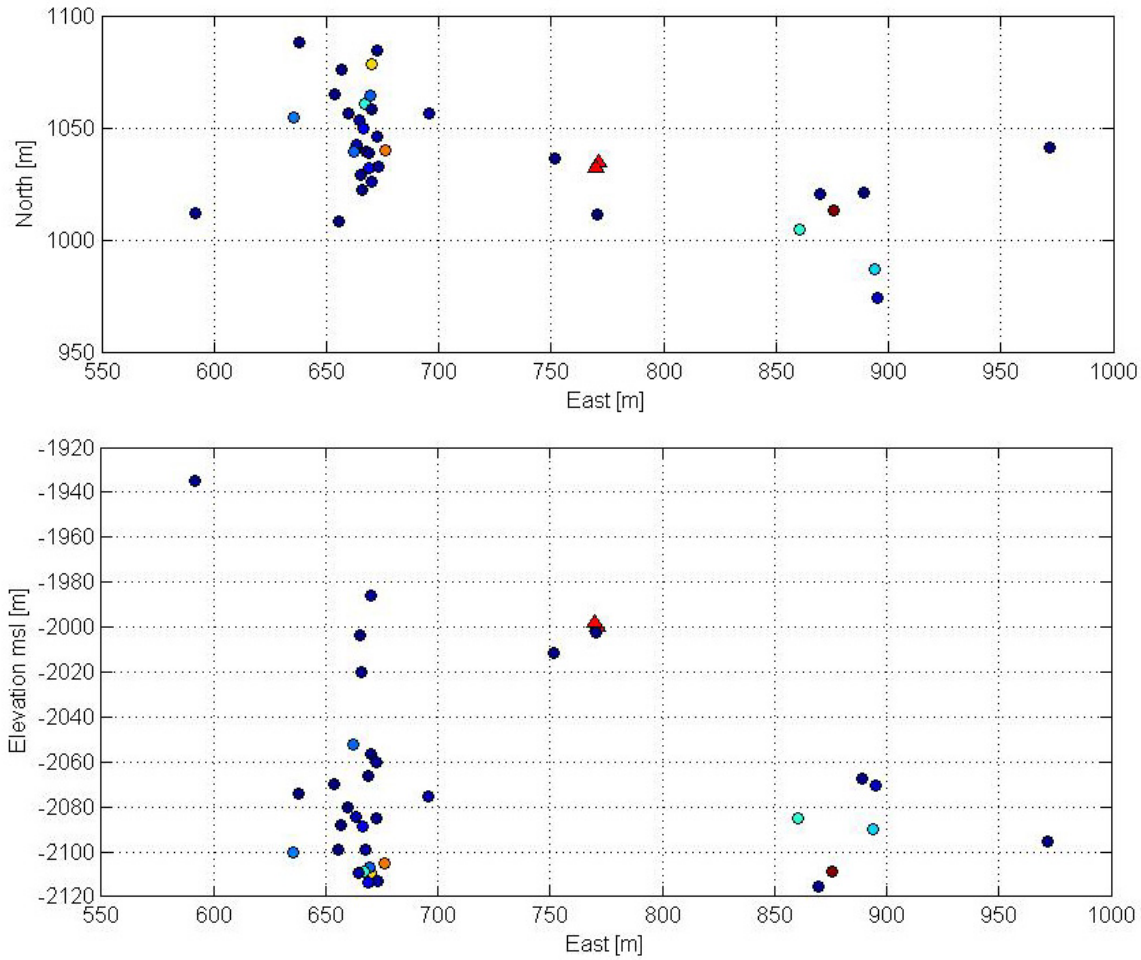

Figure 8 *Map of aftershocks following the M1.8 microearthquake. Colorbar represents the time after the event, with dark blue immediately after the event, turning yellow-red with time. Last event in this section occurred 2 hours and 37 minutes after the main shock. The red triangles depict the two MH stations. The cluster of aftershocks that are aligned about 100 m to the West of the MH stations coincides roughly with a fault zone that has been identified in the MH cuttings at 10480 feet. Coordinates are given as North and South relative to the SAFOD drill site.*

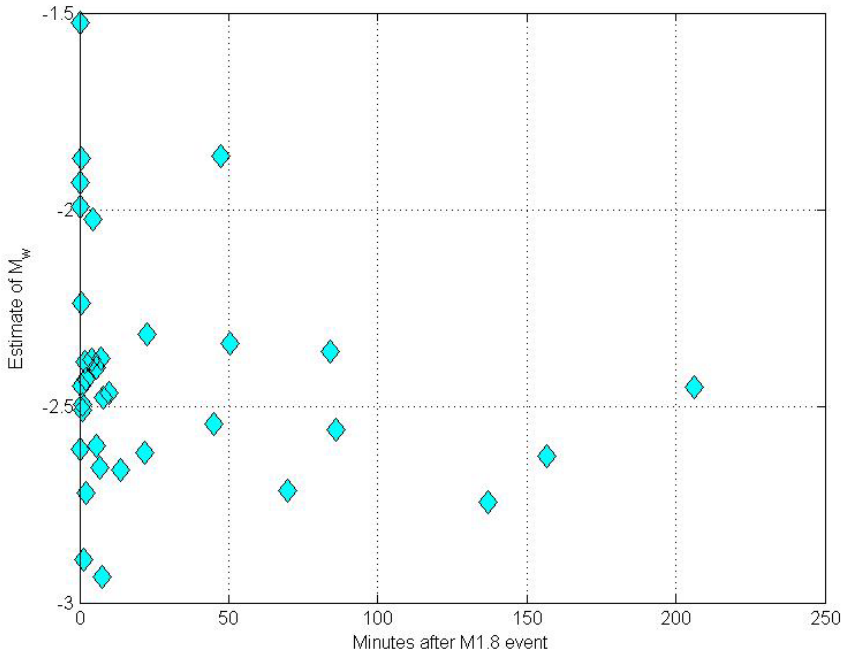

Figure 9 *Distribution of aftershocks with respect to time after main shock and an estimate of the moment magnitude M_w. The frequency of event occurrence is decreasing rapidly and follows a hyperbolical shape as indicated by Omori's law. The cumulative energy radiated by all aftershocks remains clearly below 10% of the main shock's radiated seismic energy.*

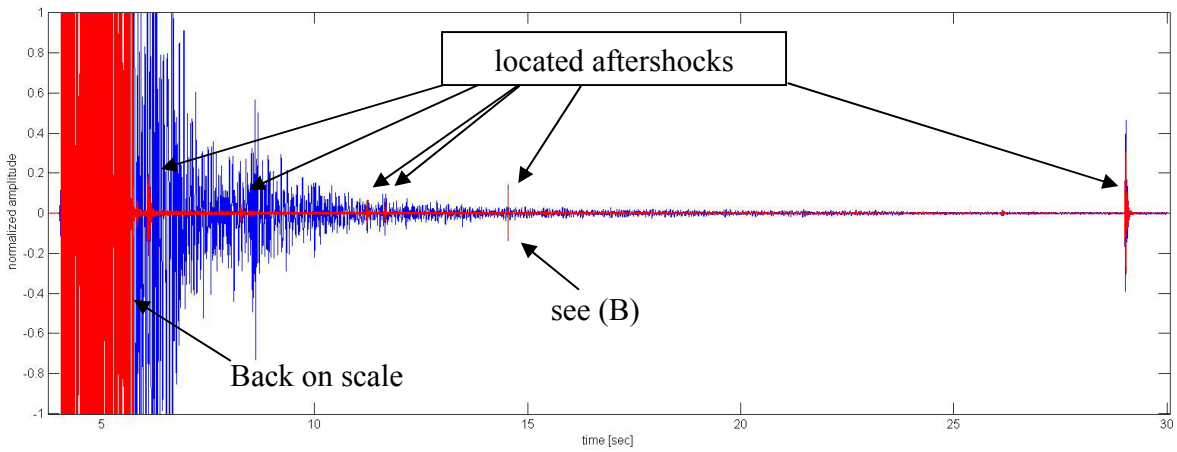

Figure 10 (A) *30 seconds of data following the M1.8 microearthquake. The blue line shows the original, unfiltered seismogram, whereas the red line is high-pass filtered with 450 Hz. After a few seconds the seismograph is back on scale and shortly after the first aftershock appears on the filtered record. Four of these aftershocks had been detected automatically and six of them were manually located later on.*

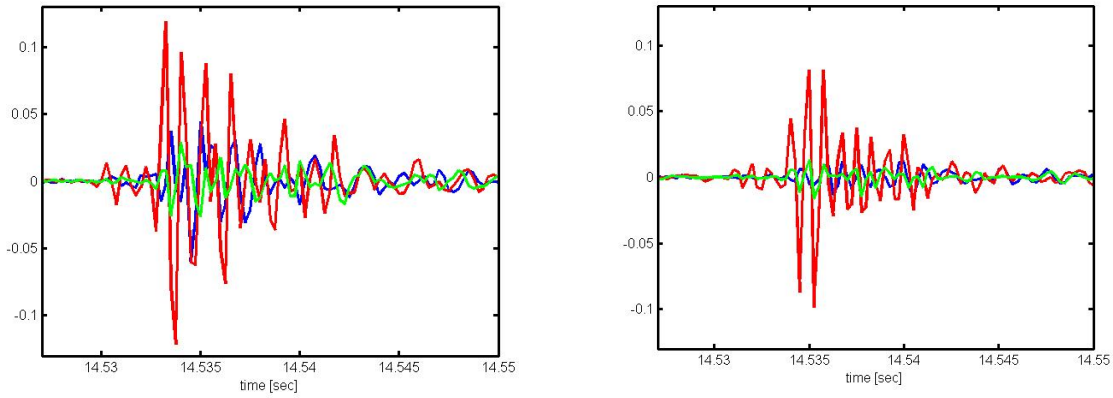

Figure 10 (B) *3-component seismogram of the micro-aftershock in (A) as recorded on the upper (left) and lower (right) MH stations. The P-wave onset time is 0.7 ms earlier on the upper station than on the lower one and the amplitudes are also slightly larger on the upper station. The event is located only about 20 m directly to the South of the MH stations at almost the same depth and is the closest event that has been located so far.*

Semiautomatic Shear wave splitting analysis

The most direct indication of anisotropy is shear-wave splitting, where the shear wave is split into two, in most cases orthogonally polarised shear-wave components, which travel at a time lag relative to each other. Such shear-wave splitting parameters as the polarisation direction of the fast wave (Φ) and the delay time (δt) of the slow wave are routinely estimated in seismology for earthquakes (e.g. Savage, 1999). Much work has been done on shear waves of specific mantle phases to deduce mantle anisotropy (e.g. Vinnik, 1989; Silver and Chang, 1991) and also a significant amount of studies have been conducted to investigate crustal anisotropy from shear-wave splitting, mostly within seismology (e.g. Crampin, 1994; Crampin and Gao, 2006).

If anisotropy is present in the upper crust, the cause for it is mostly due to structural means, such as layering, faults and their predominant direction and also due to the local stress field. In some cases clear temporal variations in the shear-wave splitting parameters were observed and interpreted to relate to changes in the local stress conditions (e.g. within an oil reservoir, here the Valhall field, North Sea, Teanby et al., 2004).

One major limitation in shear-wave splitting analyses using surface seismic stations is the angle of incidence of the S wave at the surface. If the angle of incidence is greater than about 35 º from the vertical, non-linear particle motions due to S-to-P reflections at the surface will be superposed onto the S wave signal. In the case of downhole observations, such limitations are not present and the waveform data are simply rotated into the ray coordinate system (radial and transverse components). Several automatic methods are commonly used to estimate the shear-wave splitting from the two transverse components and one of the most robust is the rotation-correlation technique (Fukao, 1984; Figure 11). In this approach a grid-search is conducted for the fast polarization direction Φ and the delay time δt, estimating the cross-correlation coefficient between the rotated and time shifted traces. Similar approaches are to maximize the aspect ratio,

to search for the minimum eigenvalue of the covariance matrix or to minimize the energy on one of the channels or to look at the polarization strength (for review see Savage, 1999; Crampin, S. and Gao, Y., 2006,). In general, all of the above methods try to improve the linearity of particle motions after applying the splitting corrections (Figure 12).

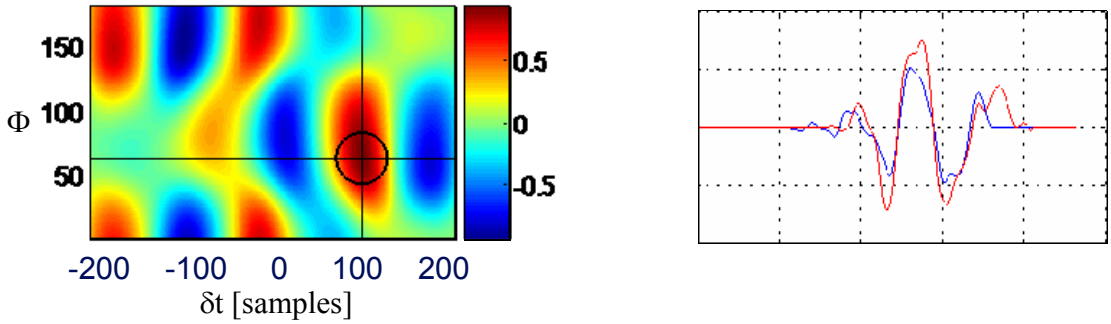

Figure 11 *Cross-correlation values for a grid search for the rotation Φ (from 1 to 180 degrees with 1 deg difference) and for the time shift δt between the components (left). The maximum value of cross-correlation is 0.918 and is at Φ = 63° and δt = 104 samples (~41.2 ms). Corresponding seismic traces for the transverse components after applying the splitting corrections (right).*

Critical parameters are the length of the analysis time window, which is optimal to start at the S-onset of the fast wave and ends after the S-onset of the slow wave. Too long time windows may result in cycle-skips, whereas too short time windows may not reveal the real extend of δt. Therefore we implemented in our semi-automatic approach the combination of the above mentioned methods, using different time windows and providing visual control on the results. A ranking of the quality can then be assigned to each measurement, in addition to automatic quality factors such as the P- and S-wave signal-to-noise ratios or the degree of agreement between the automatic methods. Another important result is the detection of null splitting, i.e. that the δt is about zero. Null splitting occurs either if the wave travelled trough an isotropic medium, or if one axis of the anisotropy is inline with the ray direction. Such detection of null splitting has often been neglected, but can be very useful for mapping of anisotropy (e.g. Wüstefeld and Bokelmann, 2006).

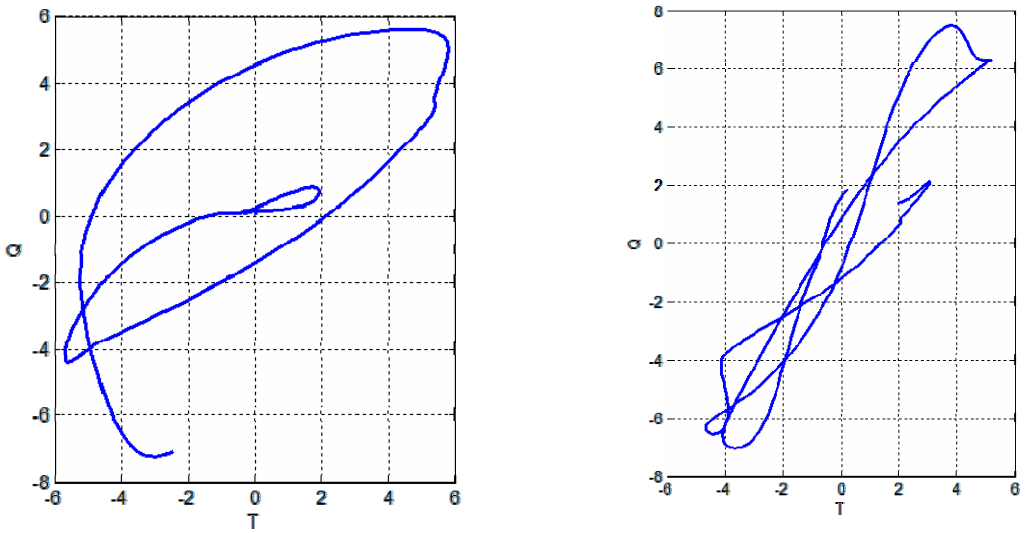

Figure 12 *Particle motion plot of a microearthquake recorded at the lower MH geophone showing the two transverse components Q and T before rotation and time shift (A) and after the correction of time shift δt 41.2 ms (equal to 103 samples) and rotation Φ of 63° (B). The elliptical shape of the hodogram in (A) is transformed into a linear relation between the two channels.*

In a first step, a selection of 35 microearthquakes have been analysed with the above mentioned automatic estimation techniques of shear wave splitting (rotation-correlation, co-variance matrix, aspect ratio and polarization strength). Only if all four methods agreed on the results of the splitting parameters, these splitting parameters for the specific source-receiver combination were accepted. As a first result, the corresponding rays are plotted with the delay times shown in absolute time and in percentages (Figure 13).

The presented results in Figure13 show significant differences in the amount of delay time with respect to the ray paths, i.e. rays penetrating the northern part of the study region, close to station SCYB, have larger delay times. Also rays travelling along the SAF in the Northeastern part of the SAF seem to have larger delay times than their Southwestern counterparts. At this time we only plotted straight rays for the visualisation, though using a 3D velocity model in the whole process of location. Therefore there could come up some changes in the details, also with respect to the penetration depth of the rays. With the correct visualisation of the rays and with more analysed data (we now only used 35 earthquakes), we hope to be able to resolve differences between the anisotropy that is due to the fault gouge of the SAF and the stress-induced anisotropy.

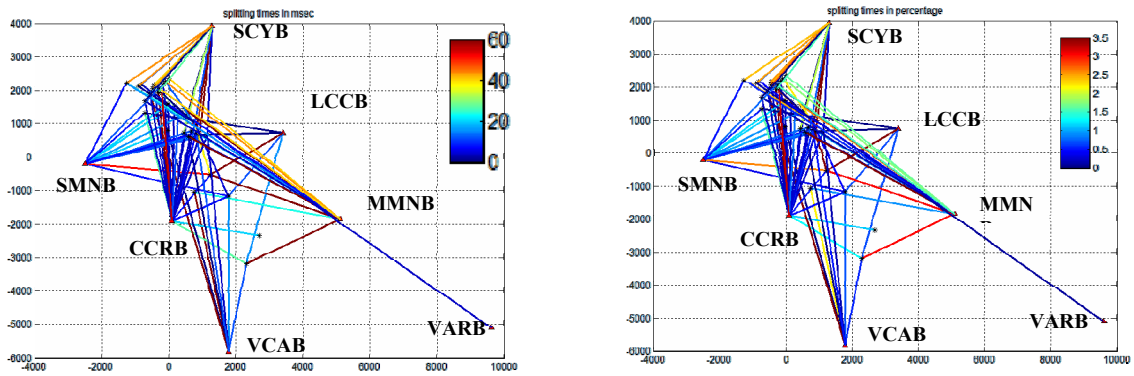

Figure 13 *Mapview of events and stations for each raypath (Coordinates are given as North and East of the SAFOD drill site in m). The color coding represents the delay time in ms (A) and in % values (B), respectively. The northern part, close to station SCYB shows significantly larger values of anisotropy than the southwestern counterpart of the SAF with stations CCRB and SMNB, showing almost null-splitting for many events.*

Concluding remarks

In this project we demonstrated that a detection processing based on the high-frequency SAFOD downhole data is significantly improving the overall detection capabilities of the combined SAFOD/HRSN seismic network. Online processing of SAFOD downhole data in combination of HRSN and NCSN detection picks as well as offline processing of combined SAFOD and HRSN waveform data has been conducted and catalogues of event detections and locations have been produced. The high-frequency SAFOD data (4000 Hz) in contrast to the downsampled data (250 Hz) that is used for standard processing within the Earthworm system, provided valuable event detections very near (about 20 to 200 m) to the SAFOD MH stations. This sequence of micro-aftershock events followed a pattern of occurrence and size that is similar to Omori's law for large earthquakes, suggesting scale invariance to some degree.

The second part in this project was related to the analysis of shear wave splitting that is related to anisotropy in the near SAFOD area. First results indicate that the amount of the splitting time is varying significantly spatially and with depth and even some nearby ray paths show rather strong differences in the amount of their splitting times. Since the amount of the splitting times is due to the summed strength of anisotropy along the ray paths, it is important to compare the real ray paths within the 3D volume, as e.g. Liu et at., (2008) have done for the larger Parkfield region. Comparing our first results, we also find that most of the delay times are due to anisotropy in the upper part of the crust and we find a volume of increased anisotropy in the North-Northwest of SAFOD. More data will need to be evaluated to enforce these speculations.

Acknowledgements
We would like to thank T. Kværna, M. Roth, D. Kühn, and H. Gharti at NORSAR, for interesting discussions about the presented topic. We also thank the SAFOD PI's W. Ellsworth, M. Zoback

and S. Hickman; L. Dietz, USGS; D. Neuhauser, BSL, and many others involved in SAFOD; S. Roecker for the access to the velocity model and H. Zhang for discussions.
Research supported by the U.S. Geological Survey (USGS), Department of the Interior, under USGS award number 07HQGR0030. The views and conclusions contained in this document are those of the authors and should not be interpreted as necessarily representing the official policies, either expressed or implied, of the U.S. Government.

References

Crampin, S., 1994. The fracture criticality of crustal rocks, Geopys. J. Int., 118, 428-438.

Crampin, S. & Gao, Y., 2006. 'A review of techniques for measuring shear-wave splitting above small earthquakes', *Physics of the Earth and Planetary Interiors* 159, 1-14.

Ellsworth, W., M. Aranha, E. Davis, L. Dietz, S. Hickman, G. Jensen, W. Kohler, R. Krug, J. Luetgert, D. Neuhauser, V. Oye, B. Prevedel, E. Samson, R. Uhrhammer, C. Weiland, M. Zoback, and M. Zumberge, 2007a. The San Andreas Fault Observatory at Depth: Monitoring Earthquakes and Fault Movement Inside the Fault., *Seismo. Res. Lett*, **78**, no. 2.

Ellsworth, W., P. Malin, K. Imanishi, S. Roecker, R. Nadeau, V. Oye, C. Thurber, F. Waldhauser, N. Boness, S. Hickman, M. Zoback, 2007b. Seismology inside the Fault Zone: Applications to Fault-Zone Properties and Rupture Dynamics, in Scientific Drilling, Special Issue, No.1, 2007, ISSN: 1816-8957.

Fukao, Y., 1984. Evidence from core-reflected shear waves for anisotropy in the earth's mantle, Nature, 309, 695-698.

Hickman, S., M. D. Zoback, and W. Ellsworth (2004). Introduction to special sections: Preparing for the San Andreas Fault Observatory at Depth, *Geophys. Res. Lett.* **31**, L12S01.

Imanishi, K., and W. L. Ellsworth, 2006, Source Scaling Relationships of Microearthquakes at Parkfield, CA, Determined Using the SAFOD Pilot Hole Seismic Array, in Earthquakes: Radiated Energy and the Physics of Faulting. Abercrombie, R., A. McGarr, and H. Kanamori, Eds., Geophysical Monograph Series, **170**, Amer. Geophys U., 81-90.

Liu, Y., H. Zhang, C. Thurber & S. Roecker, 2008. Shear wave anisotropy in the crust around the San Andreas fault near Parkfield: spatial and temporal analysis, *Geophys. J. Int.*, 172, 957-970 doi:10.1111/j.1365-246X.2007.03618.x

Oye, V., H. Bungum, and M. Roth, 2005. Source parameters and scaling relations for mining related seismicity within the Pyhäsalmi ore mine, Finland. *Bull. Seism. Soc. Am.* **95**, 3, 1011-1026, doi: 10.1785/0120040170.

Oye, V., J. A. Chavarria, and P. E. Malin (2004). Determining SAFOD area microearthquake locations solely with Pilot Hole seismic array data, *Geophys. Res. Lett.* **31**, L12S10, doi:10.1029/2003GL019403.

Oye, V., Roth, M., 2003. Automated seismic event location for hydrocarbon reservoirs, *Computers & Geoscience* **29**, 851-863.

Ringdal, F., and T. Kværna, 1992. Continuous seismic threshold monitoring, *Geophys. J. Int.* **111**, 505-514.

Savage, M. K., 1999. Seismic anisotropy and mantle deformation: what have we learned from shear wave splitting? Reviews of Geophysics, 37, 65-106.

Silver, P. G. and W. W. J. Chan, 1991. Shear-wave splitting and subcontinental mantle deformation, J. Geophys. Res., 96, 16,429-16,454.

Teanby, N. A., J.-M. Kendall, R.H. Jones, and O. Barkved, 2004. Stress-induced temporal variations in seismic anisotropy observed in microseismic data, Geophys. J. Int., 156, 459-66.
Thurber, C., S. Roecker, H. Zhang, S. Baher, and W. Ellsworth (2004). Fine-scale structure of the San Andreas fault zone and location of the SAFOD target earthquakes, *Geophys. Res. Lett.* **31**, L12S02, doi:10.1029/2003GL019398.
Unsworth, M., and P. A. Bedrosian (2004). Electrical resistivity at the SAFOD site from magnetotelluric exploration, *Geophys. Res. Lett.* **31**, L12S05, doi:10.1029/2003GL019405
Vinnik, L. P., R. Kind, G. L. Kosarev, and L. I. Makeyeva, 1989. Azimuthal anisotropy in the lithosphere from observations of long-period S-waves, Geophys. J. Int., 99, 549-559.
Wüstefeld, A. and G. Bokelmann, 2007. Null Detection in Shear-Wave Splitting Measurements, Bull. Seism. Soc. Am., 97, 4, 1204-11, doi: 10.1785/0120060190.

Bibliography

Oye, V., 2008. Shear-wave Splitting Analysis of Microearthquake Data Observed with Downhole Seismic Network, EAGE extended abstract, Rome, Italy.

Oye, V., W. E. Ellsworth, 2007. Small-Scale Structures Derived From Microearthquake Locations Using SAFOD and HRSN Data, Eos Trans. AGU, 88(52), Fall Meet. Suppl., Abstract T53C-03.

Oye, V., W. E. Ellsworth, 2007. Monitoring Microearthquakes with the San Andreas Fault Observatory at Depth, EAGE extended abstract, London, UK.

The presented report will also serve as a draft manuscript to be submitted shortly to either Geophysical Journal International or Journal of Geophysical Research.

Annex A

Waveform plots of some typical recorded events:
Showing channels
1: SAFOD PH
2-3 SAFOD MH
4 -16 HRSN

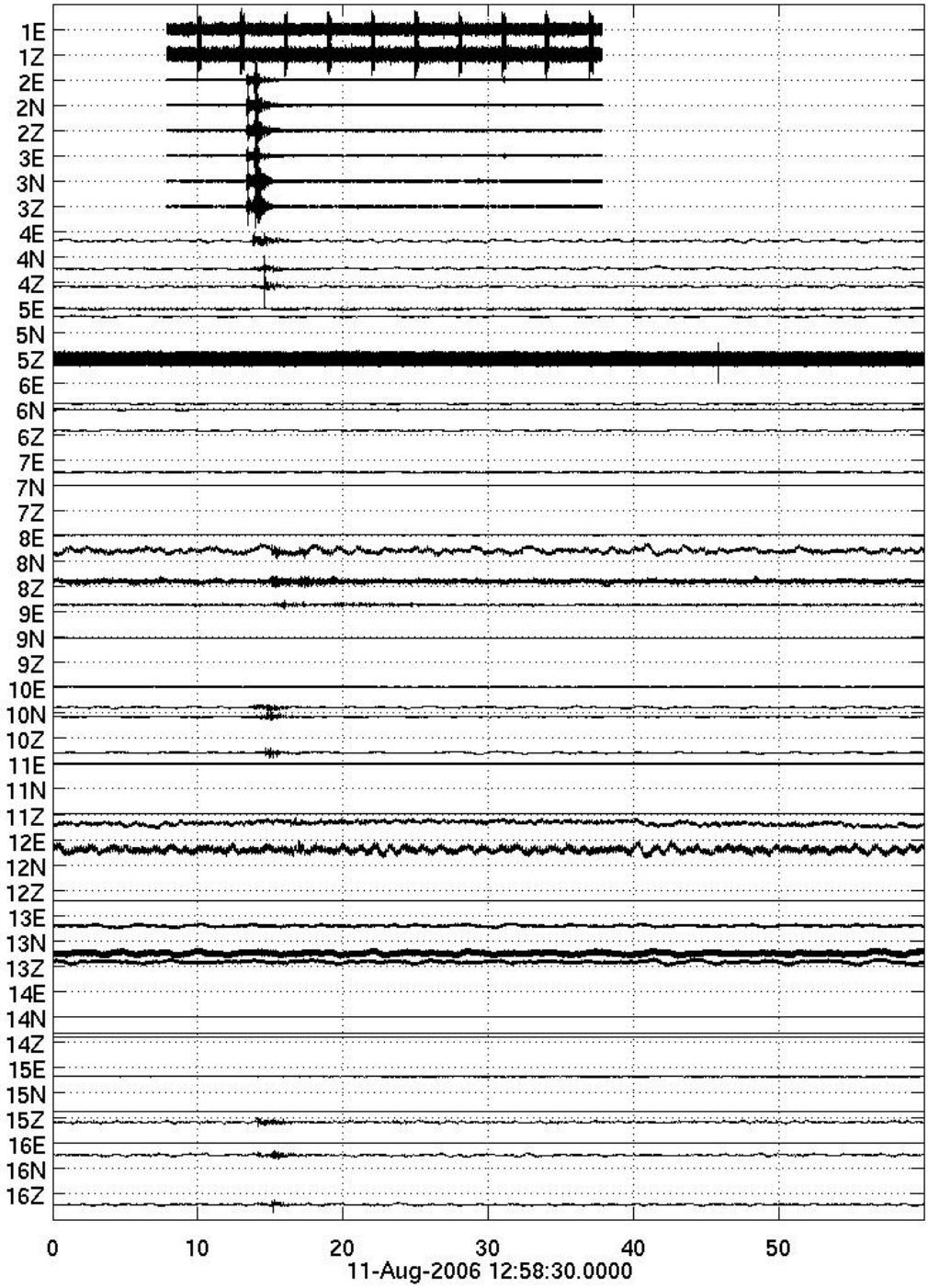
1E
1Z
2E
2N
2Z
3E
3N
3Z
4E
4N
4Z
5E
5N
5Z
6E
6N
6Z
7E
7N
7Z
8E
8N
8Z
9E
9N
9Z
10E
10N
10Z
11E
11N
11Z
12E
12N
12Z
13E
13N
13Z
14E
14N
14Z
15E
15N
15Z
16E
16N
16Z
0
10
20
30
40
50
11-Aug-2006 12:58:30.0000

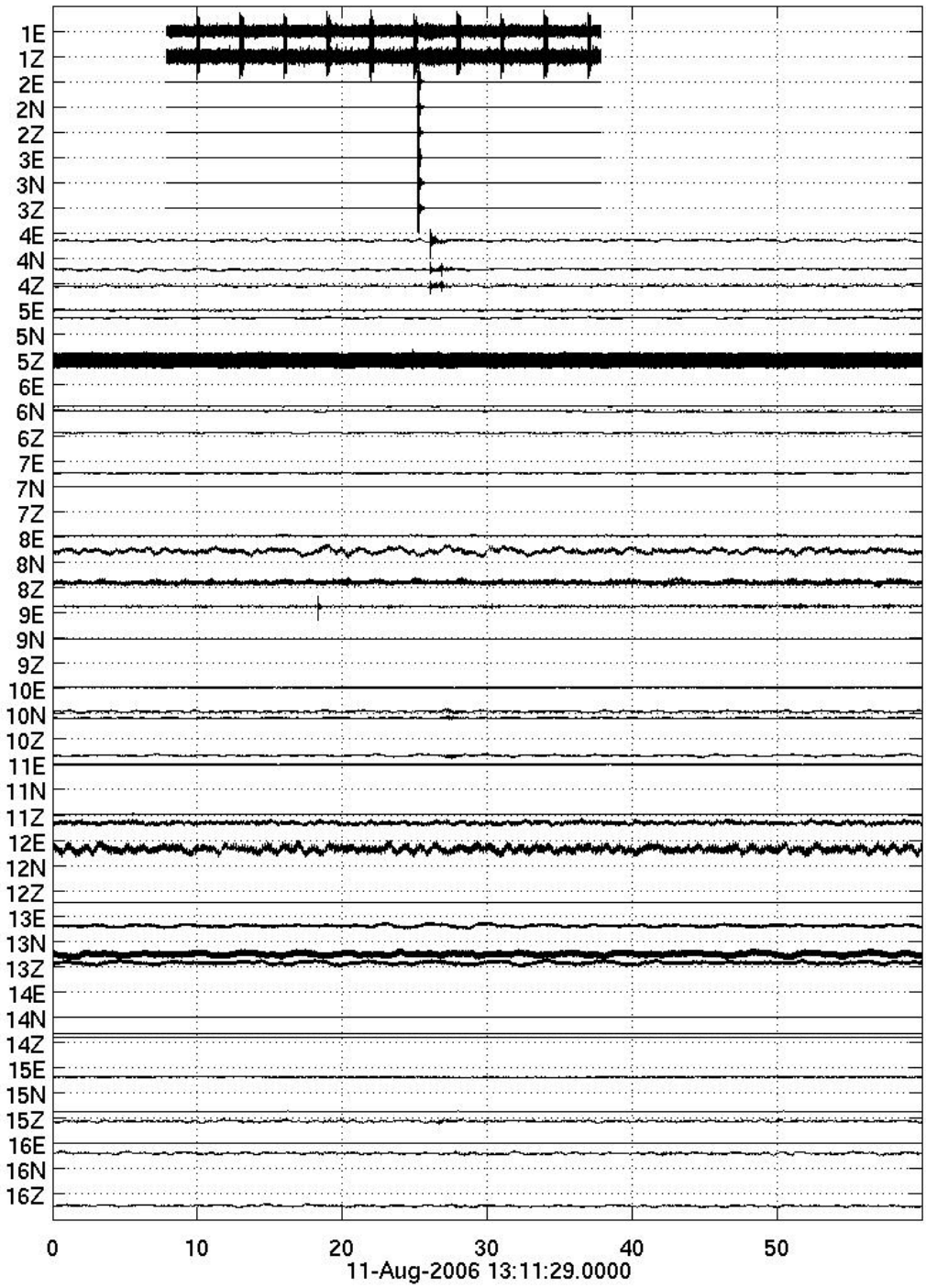
1E
1Z
2E
2N
2Z
3E
3N
3Z
4E
4N
4Z
5E
5N
5Z
6E
6N
6Z
7E
7N
7Z
8E
8N
8Z
9E
9N
9Z
10E
10N
10Z
11E
11N
11Z
12E
12N
12Z
13E
13N
13Z
14E
14N
14Z
15E
15N
15Z
16E
16N
16Z
0
10
20
30
40
50
11-Aug-2006 13:11:29.0000

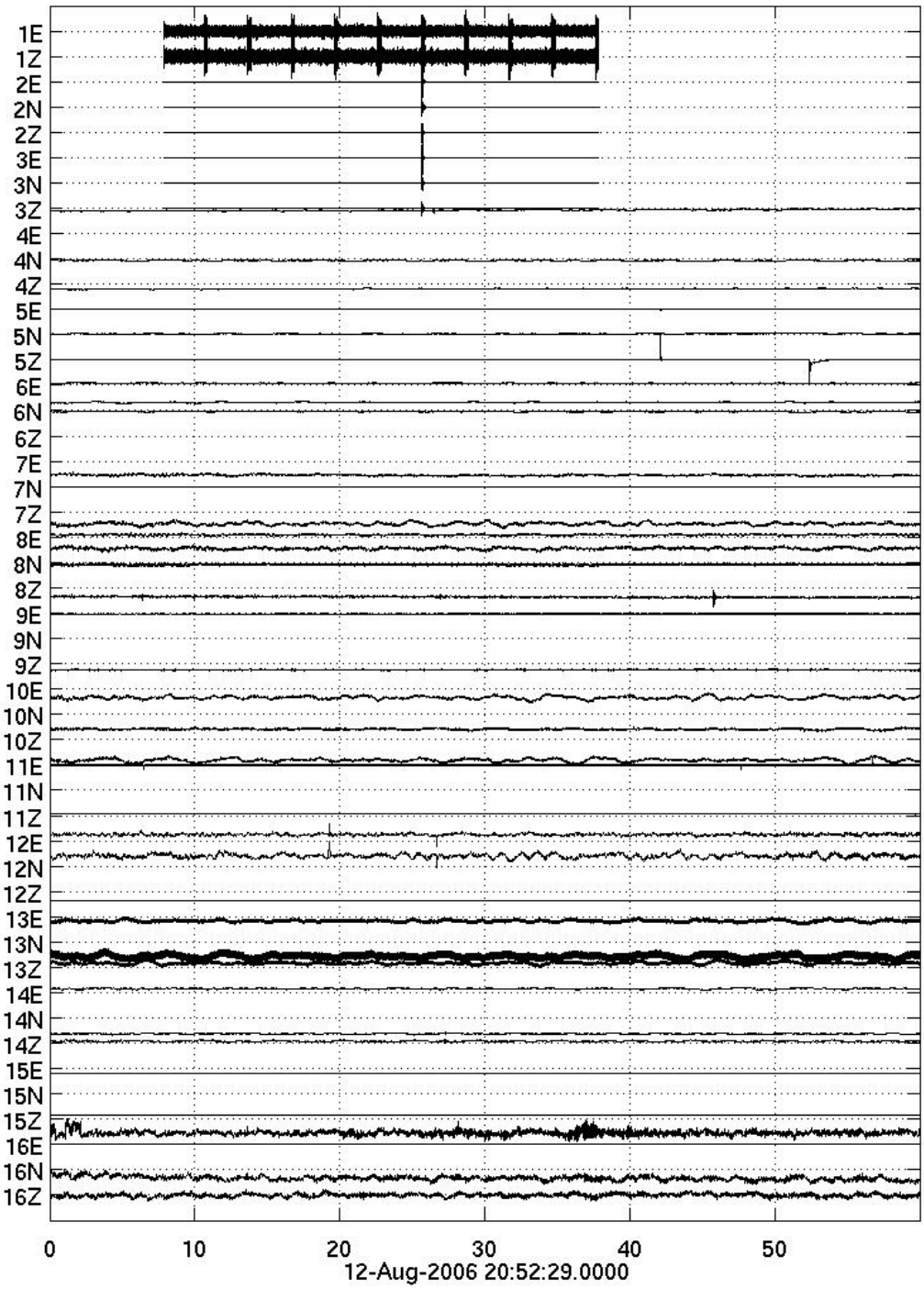
1E
1Z
2E
2N
2Z
3E
3N
3Z
4E
4N
4Z
5E
5N
5Z
6E
6N
6Z
7E
7N
7Z
8E
8N
8Z
9E
9N
9Z
10E
10N
10Z
11E
11N
11Z
12E
12N
12Z
13E
13N
13Z
14E
14N
14Z
15E
15N
15Z
16E
16N
16Z
0
10
20
30
40
50
12-Aug-2006 20:52:29.0000

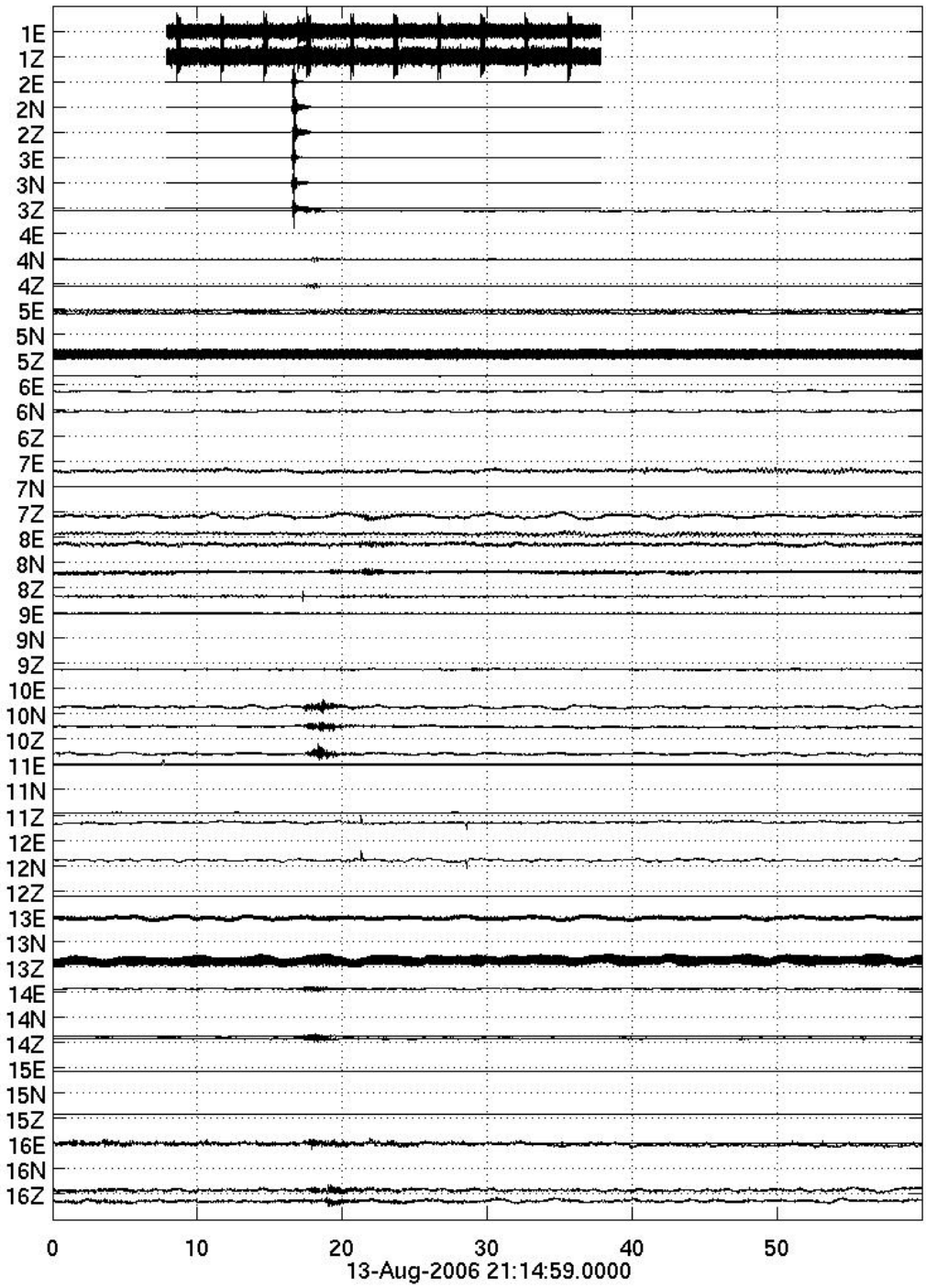
1E
1Z
2E
2N
2Z
3E
3N
3Z
4E
4N
4Z
5E
5N
5Z
6E
6N
6Z
7E
7N
7Z
8E
8N
8Z
9E
9N
9Z
10E
10N
10Z
11E
11N
11Z
12E
12N
12Z
13E
13N
13Z
14E
14N
14Z
15E
15N
15Z
16E
16N
16Z
0
10
20
30
40
50
13-Aug-2006 21:14:59.0000

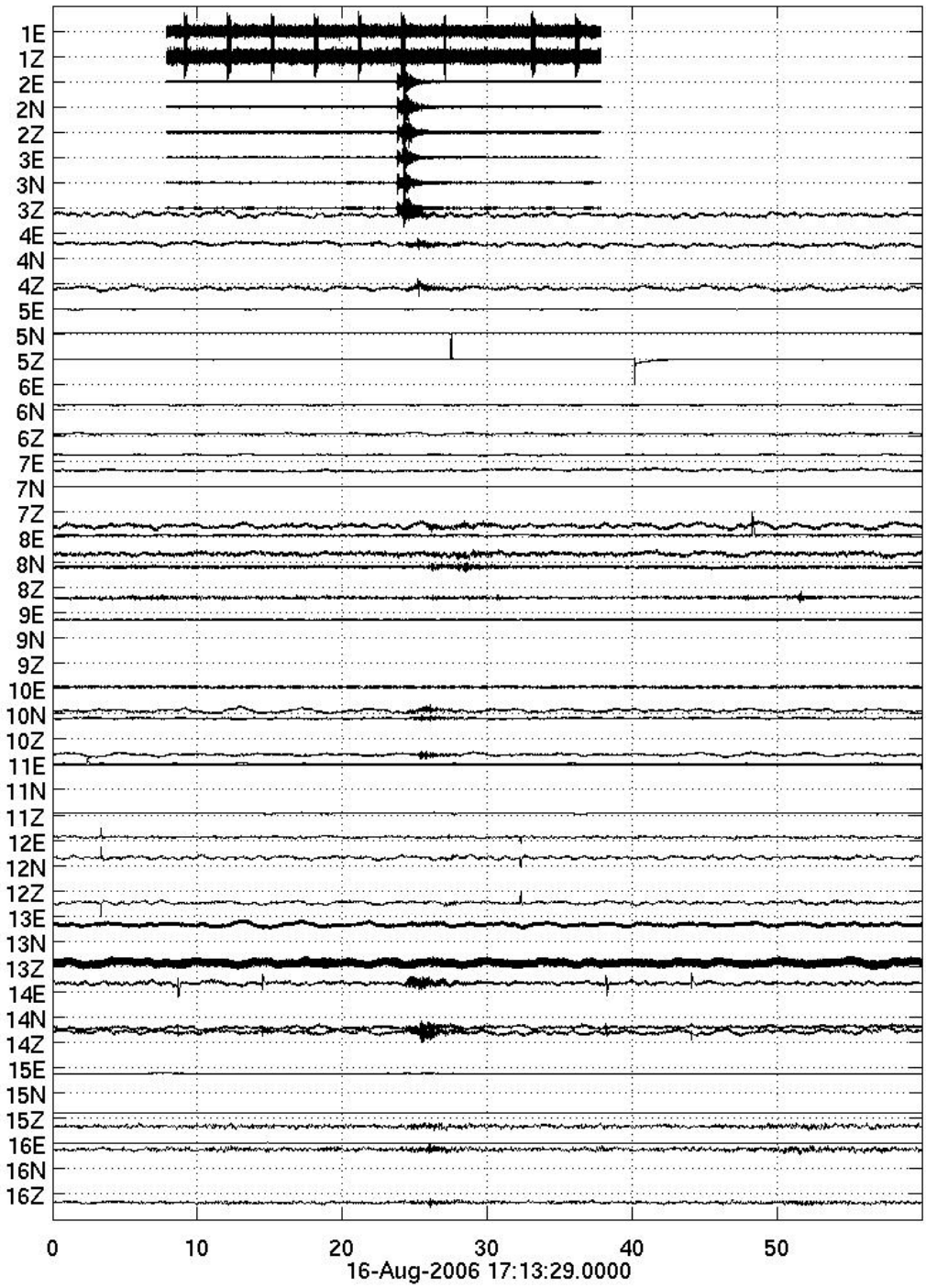
1E
1Z
2E
2N
2Z
3E
3N
3Z
4E
4N
4Z
5E
5N
5Z
6E
6N
6Z
7E
7N
7Z
8E
8N
8Z
9E
9N
9Z
10E
10N
10Z
11E
11N
11Z
12E
12N
12Z
13E
13N
13Z
14E
14N
14Z
15E
15N
15Z
16E
16N
16Z
0
10
20
30
40
50
16-Aug-2006 17:13:29.0000

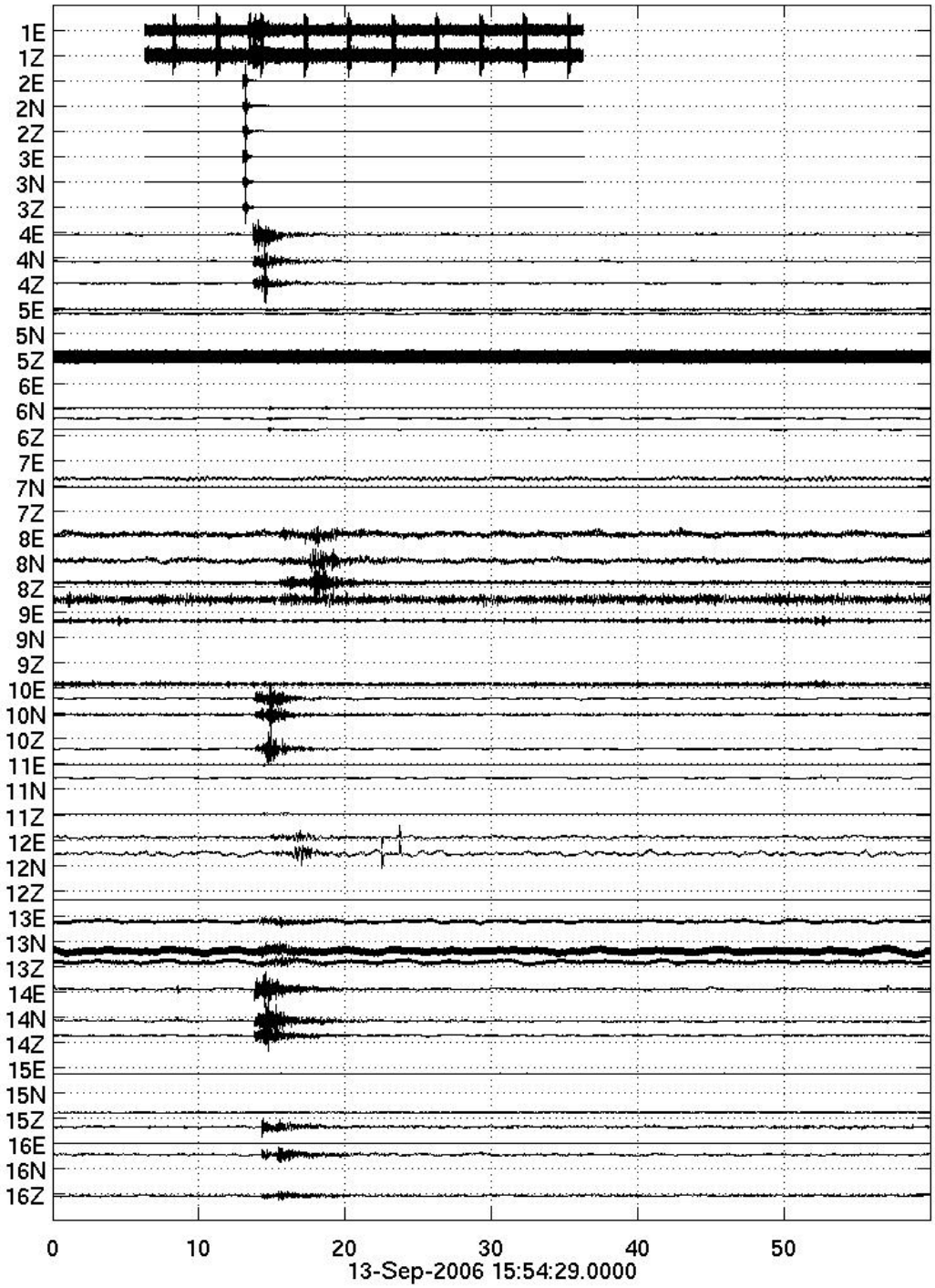
1E
1Z
2E
2N
2Z
3E
3N
3Z
4E
4N
4Z
5E
5N
5Z
6E
6N
6Z
7E
7N
7Z
8E
8N
8Z
9E
9N
9Z
10E
10N
10Z
11E
11N
11Z
12E
12N
12Z
13E
13N
13Z
14E
14N
14Z
15E
15N
15Z
16E
16N
16Z
0
10
20
30
40
50
13-Sep-2006 15:54:29.0000